J Solid State Electrochem (2012) 16:3651–3659
DOI 10.1007/s10008-012-1809-1

ORIGINAL PAPER

The effects of crystal structure of the precursor MnO_2 on electrochemical properties of spinel $LiMn_2O_4$

Qiliang Wei · Xianyou Wang · Xiukang Yang · Hongbo Shu · Bowei Ju · Benan Hu · Yunfeng Song

Received: 8 May 2012 / Revised: 22 June 2012 / Accepted: 24 June 2012 / Published online: 6 July 2012

Abstract The spinel $LiMn_2O_4$ samples for lithium-ion battery have been synthesized through one-step solid-state method using four different polymorphs of MnO_2, e.g., α-, β-, γ-, and δ-MnO_2. The structure, morphology, and electrochemical properties of as-prepared $LiMn_2O_4$ were characterized by X-ray diffraction, X-ray photoelectron spectroscopy, scanning electron microscope, galvanostatic charge/discharge, cyclic voltammogram, and electrochemical impedance spectroscopy. The results reveal that the performances of as-prepared $LiMn_2O_4$ are obviously affected by crystal structure of MnO_2 precursor. Among all as-prepared $LiMn_2O_4$, the $LiMn_2O_4$ sample obtained from β-MnO_2 shows the best electrochemical performance. The initial discharge capacity is 126 mAh g^{-1} at 0.5 C (74 mA g^{-1}) between 3.0 and 4.4 V; after 100 cycles, its capacity retention is still 83.3 %.

Keywords Lithium-ion battery · Spinel $LiMn_2O_4$ · MnO_2 crystal structure · Electrochemical properties

Introduction

The electric vehicle using a rechargeable lithium-ion battery is seen as one of the ways to solve two great problems of industry: the shortage of oil energy sources and the pollution of the environment [1]. Spinel lithium manganese oxide ($LiMn_2O_4$) is currently one of the most promising cathodes for lithium-ion batteries because of abundant manganese resources, environmental friendliness, low cost, and facile production. However, the spinel $LiMn_2O_4$ suffers from capacity fading during cycling due to crystal distortion, which has been a key problem prohibiting $LiMn_2O_4$ from commercialization. Several contributing factors could include Jahn–Teller distortion, e.g., lattice instability, manganese dissolution, and electrolyte decomposition [2–6]. Thus, a great deal efforts have been done for obviating these defects. For example, metal doping at the Mn-site and metal oxide coating on the surface have been successfully used to avoid Mn-dissolution [7–13].

On the other hand, it is well-known that the structure and morphology of the starting materials, reaction temperature and time, and the preparation technique have a great impact on the electrochemical properties of $LiMn_2O_4$ [14, 15]. An important class of the starting materials for the preparation of $LiMn_2O_4$ is the manganese dioxides, MnO_2, of which there are over 14 polymorphs [16]. Several kinds of MnO_2 have usually been chosen as the manganese source to obtain spinel $LiMn_2O_4$, for example, electrolytic manganese dioxide has been widely used as manganese compound for synthesis of $LiMn_2O_4$ cathode; however, due to existence of the impurities such as Na^+ and SO_4^{2-}, the maximum initial discharge capacity is 117 mAh g^{-1} at a rate of 0.2 C with a capacity retention of 93.5 % at the 15th cycle [17–23]. Besides, Luiz C et al. used ε-MnO_2 as Mn source to get the spinel $LiMn_2O_4$; the initial discharge capacity was about 110 mAh g^{-1} at a rate of 0.36 C [24], Bao et al. optimized the spinel $LiMn_2O_4$ using γ-MnOOH [17]; the initial discharge capacity was 115 mAh g^{-1} at C/3. Jae Won Lee et al. prepared the $LiMn_2O_4$ using different CMDs, and obtained a capacity of about 110 mAh g^{-1} at 0.1 C [25].

In order to study systematically the effects of crystal structure of MnO_2 precursor on the electrochemical performances of spinel $LiMn_2O_4$, in this study, four different polymorphs of MnO_2, for example, α-, β-, γ-, and δ-MnO_2, have been selected as the manganese source to obtain

Q. Wei · X. Wang (✉) · X. Yang · H. Shu · B. Ju · B. Hu · Y. Song
School of Chemistry, Key Laboratory of Environmentally Friendly Chemistry and Applications of Ministry of Education,
Xiangtan University,
Xiangtan, Hunan 411105, China
e-mail: wxianyou@yahoo.com

spinel-structured $LiMn_2O_4$ through one-step solid-state reaction. The microstructure and electrochemical properties of the synthesized samples are characterized and discussed in detail.

Experimental

Synthesis of MnO_2 polymorphs

All the chemicals are of analytical grade and used without further purification. The preparation methods of different crystal structure MnO_2 polymorphs are as follows:

1. δ-MnO_2. A solution containing 0.2 M $(NH_4)_2S_2O_8$ was slowly added to the solution (100 mL) consisting of 0.2 M $MnSO_4{\cdot}H_2O$ and 1.2 M NaOH for about 10 h, and filtered. The precipitate obtained, after thorough rinsing with deionized water until nearly there is no SO_4^{2-}, was dried at 100 °C for 6 h [26].
2. α-MnO_2. To obtain precipitate powder of α-MnO_2, $K_2S_2O_8$ as an oxidizer was added into hot 1 M $MnSO_4{\cdot}H_2O$ aqueous solution. The precipitated product was filtered and washed with deionized water followed by drying in air at 80 °C [27].
3. γ-MnO_2. A solution (100 mL) consisting of 0.84 M $Na_2S_2O_8$ and 0.84 M $MnSO_4{\cdot}H_2O$ was heated to the boiling point for about 5 min, cooled, and filtered. The precipitate obtained, after thorough rinsing with deionized water until the resulting pH was near 7, was dried at 55 °C for 12 h [28].
4. β-MnO_2. By heating the aforementioned γ-MnO_2 at 300 °C for 12 h, β-MnO_2 was prepared [29].

Preparation of $LiMn_2O_4$ using α-, β-, γ-, and δ-MnO_2

$LiMn_2O_4$ powder was synthesized by the one-step solid-state method. A stoichiometric amount of Li_2CO_3 and manganese dioxide was mixed by grinding in the agate mortar with ethanol as the dispersing agent. The obtained precursors were annealed at 750 °C for 24 h [30] followed by slow cooling to room temperature.

Structure and morphology characterization

The structures of synthesized samples were characterized by X-ray powder diffraction using a Rigaku D/MAX-2500 powder diffractometer with a graphite monochromatic and Cu Kα radiation (λ=0.15418 nm) in the 2θ range of 10–70°. The lithium content of the products was examined with a Perkin–Elmer atomic absorption spectrometer with a lithium lamp (Beckman) operating at λ=670 nm. The X-ray photon spectra of O 1 s and Mn 2p were recorded by X-ray photoelectron spectroscopy (XPS) with monochromatic Al Kα radiation at 1,450 eV. The spectra were scanned in the range from 0.01 to 1,400 eV binding energy in 0.5 eV steps. The surface morphology of the samples was observed using the JSM-5600LV scanning electron microscope (SEM) (JEOL, Japan).

Electrochemical evaluation

The cathode for lithium cells was fabricated by mixing the active material, carbon black, and polyvinylidene fluoride binder in a weight ratio of 80:10:10 in *N*-methyl pyrrolidinone. The slurry was coated onto an aluminum foil and dried under vacuum at 110 °C overnight. The testing cells were assembled with the cathodes thus fabricated, metallic lithium anode, Celgard 2400 film separator, and 1 M $LiPF_6$ in 1:1 ethylene carbonate/dimethyl carbonate electrolyte. The assembly of the testing cells was carried out in an argon-filled glove box, where water and oxygen concentration were kept less than 5 ppm. Charge–discharge measurement was carried out in Neware battery test system BTS-XWJ-6.44 S-00052 (Newell, Shenzhen, China) at different current densities between 3.0 and 4.4 V vs. Li^+/Li at room temperature. All the tests were performed at room temperature. Cyclic voltammetry (CV) tests and electrochemical impedance spectroscopy experiments were performed on a Zahner Zennium electrochemical workstation (Zahner, Germany). CV tests were carried out at a scan rate of 0.1 mV s^{-1} on the potential interval 3.0–4.4 V (vs. Li^+/Li). The ac perturbation signal was ±5 mV and the frequency range was from 10 to 10 KHz.

Results and discussion

Characteristics of different polymorphs MnO_2 and corresponding $LiMn_2O_4$

Figure 1 shows the X-ray diffraction (XRD) patterns of the as-prepared MnO_2, which are matched to the JCPDS of δ-, α-, γ-, and β-MnO_2 respectively. It can be seen from Fig. 1 that all as-prepared MnO_2 samples were the same as the pro-designated crystal structure no matter what the preparing technology is used.

The XRD patterns of the spinel $LiMn_2O_4$ samples prepared from δ-, α-, γ-, and β-MnO_2 are presented in Fig. 2. The result indicates that four samples have identical crystal structures. All the diffraction peaks can ascribe to the cubic spinel structure with space group Fd3m, wherein the lithium ions occupy 8*a* sites, manganese ions 16*d* sites, and oxygen ions 32*e* sites. The diffraction pattern is in good agreement with the JCPDS standard (JCPDS 35–0782). No other crystal phase or obvious impurity peaks are detected. However,

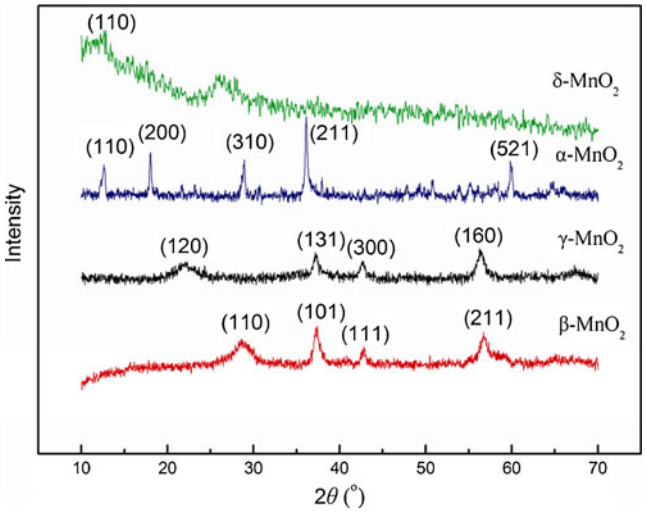

Fig. 1 XRD patterns of the four polymorphs MnO_2

there are some slight different characteristics among these $LiMn_2O_4$ materials; the lattice constant a of $LiMn_2O_4$ prepared from δ-, α-, γ-, and β-MnO_2 are 8.241, 8.250, 8.248, and 8.247 Å, respectively, which indicates that the unit cell parameters are affected by the starting materials to some extent. It should also be noted that the ratio value of the (3:1:1)/(4:0:0) peaks reflects the structural stability of the $[Mn_2]O_4$ spinel framework [17, 31]. The tiny structural difference between the samples may result from the different starting materials. Therefore, the structural difference resulting from the intensity ratio of (3:1:1)/(4:0:0) peaks may be closely related to the electrochemical properties of spinel lithium manganese oxide. The (3:1:1)/(4:0:0) peak intensity ratio (R), obtained for the sample prepared from β-MnO_2 (R=0.92) is lower than the other three samples (Fig. 2), and it is known from the literature [32–34] that the extent of site exchange between Li and Mn atoms decreases with a decrease in the (3:1:1)/(4:0:0) intensity ratio. Therefore, it is expected from the $LiMn_2O_4$ prepared from β-MnO_2 to show better electrochemical performance than other samples. Obviously, the structural difference of $LiMn_2O_4$ is influenced by the starting materials.

From the XRD patterns, it can be seen that the as-prepared materials are single-phase spinel $LiMn_2O_4$; all the lithium in the various samples is contained only in the $Li_xMn_2O_4$ spinel phase from the atomic absorption measurement; x of $Li_xMn_2O_4$ prepared from δ-, α-, γ-, and β-MnO_2 are 0.992, 0.998, 1.003, and 0.995, respectively, which indicates that the lithium content of all $Li_xMn_2O_4$ samples is nearly consistent.

XPS is a well-adapted, non-destructive technique for the evaluation of valence states of the metal/nonmetal ions in solids, and it has been extensively used to study the electronic structure of materials. The XPS binding energies provide useful information on the oxidation states of different elements in materials. The XPS spectra of O 1 s and Mn 2p of $LiMn_2O_4$ prepared from different polymorphs of MnO_2 are shown in Figs. 3 and 4. The binding energy of O 1 s is shown to be 529.4, 529.6, 529.9, and 530.1 eV, respectively. It can be seen that the binding energy of O 1 s shifts to higher value in the order of the samples prepared from δ-, α-, γ-, and β-MnO_2, and it can be ascribed to the stronger Mn–O bonds. [35] Another O 1 s peak at about 531 eV corresponds to the absorbed oxygen, which come from surface CO_3^{2-} and –OH, a common impurity at the surface of air exposed materials, resulting from the adsorption of CO_2 and H_2O from the ambient either upon storage or during synthesis process [36]. The Mn $2p_{3/2}$ binding energies of the samples prepared from δ-, α-, γ-, and β-MnO_2 are found to be 642.2, 642.3, 642.5, and 642.7 eV,

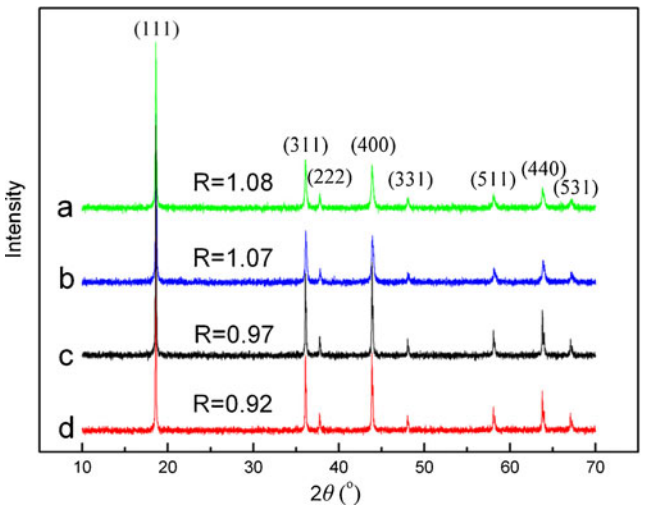

Fig. 2 XRD patterns of the four $LiMn_2O_4$ prepared from (*a*) δ-MnO_2, (*b*) α-MnO_2, (*c*) γ-MnO_2 (*d*) β-MnO_2. R is the intensity ratio of the (3:1:1)/(4:0:0) peaks

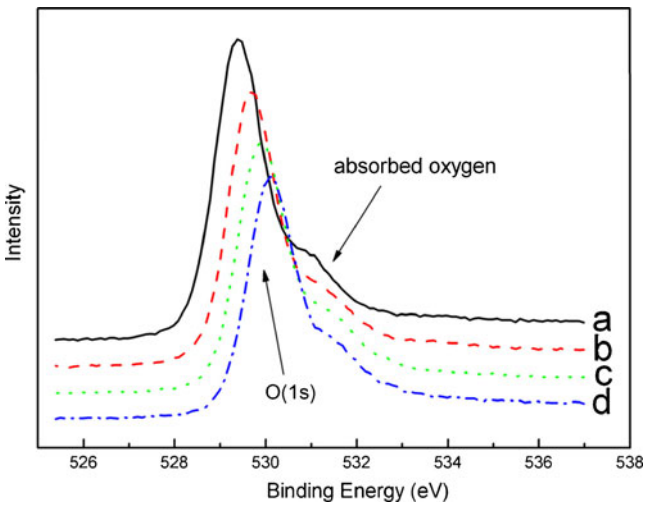

Fig. 3 O 1 s XPS spectrum of the $LiMn_2O_4$ spinel prepared from (*a*) δ-MnO_2, (*b*) α-MnO_2, (*c*) γ-MnO_2, and (*d*) β-MnO_2

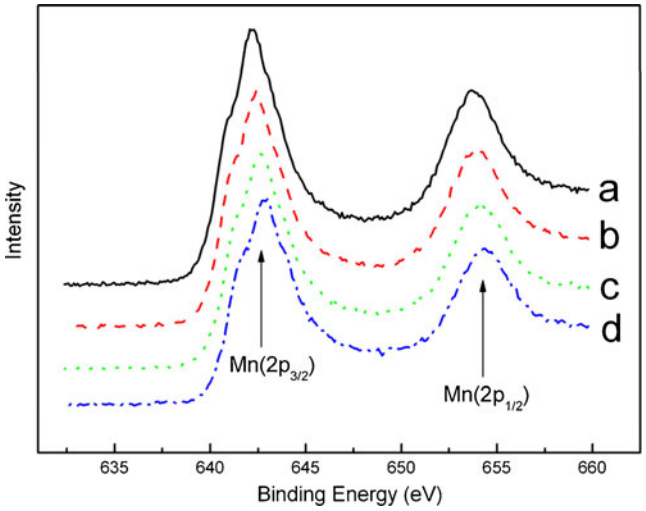

Fig. 4 Mn 2p XPS spectrum of the $LiMn_2O_4$ spinel prepared from (*a*) δ-MnO_2, (*b*) α-MnO_2, (*c*) γ-MnO_2, and (*d*) β-MnO_2

respectively. It has been reported that the Mn $2p_{3/2}$ binding energies of Mn^{3+} and Mn^{4+} are 641.9 and 643.2 eV, respectively [37]. In this study, the Mn $2p_{3/2}$ binding energies of these samples are in this region, indicating that the Mn oxidation state is between +3 and +4. Moreover, the binding energy of Mn $2p_{3/2}$ increases from 642.2 to 642.7 eV, which indicates that the average valence state of Mn ions increase following the order of the $LiMn_2O_4$ samples prepared from δ-MnO_2<α-MnO_2<γ-MnO_2<β-MnO_2, [38] while the increase of Mn^{4+} content could improve the stability of the spinel structure [39], thus the electrochemical cycle stability of the samples prepared from γ- and β-MnO_2 are expected to be better. This conclusion is consistent with the analysis of XRD.

The particle size and morphology of all the prepared samples were examined by SEM. Figure 5 shows the images of different polymorphs of MnO_2. It can be seen that all the samples are homogeneous; the difference is only their crystallinity. δ-MnO_2 presents a poor crystallinity, whereas α-MnO_2 shows a good crystallinity. The images of $LiMn_2O_4$ obtained from different polymorphs of MnO_2 are shown in Fig. 6. It can be found from Fig. 6 that the average sizes of all the samples are about 200–300 nm. Usually, the particle size and surface morphology are important factors for influencing the cycling performance of the Li/$LiMn_2O_4$ cells. Obviously, the sample prepared from β-MnO_2 (Fig. 6d) has well-distributed dispersity and very smooth surface, while other three samples show the indication of particle aggregation to some extent. Hence, β-MnO_2 is a better Mn source to obtain the $LiMn_2O_4$ sample with good crystal structure and morphology.

Electrochemical analysis of the spinel $LiMn_2O_4$

Figure 7 shows the charge/discharge curves of $LiMn_2O_4$ obtained from different polymorphs of MnO_2. It can be apparently seen that the charge/discharge curves of all the samples have two voltage plateaus at approximately 3.9 and 4.1 V, which indicates a remarkable characteristic of a well-defined spinel $LiMn_2O_4$. The two voltage plateaus manifest that the insertion and extraction of lithium ions occur in two stages [18]. In comparison with the other three samples, the sample prepared from β-MnO_2 delivers a large initial discharge capacity of 126 mAh g^{-1} (85.1 % of the theoretical value), while the other three samples show a smaller capacity of 103, 104, and 117 mAh g^{-1}, respectively. The coulombic

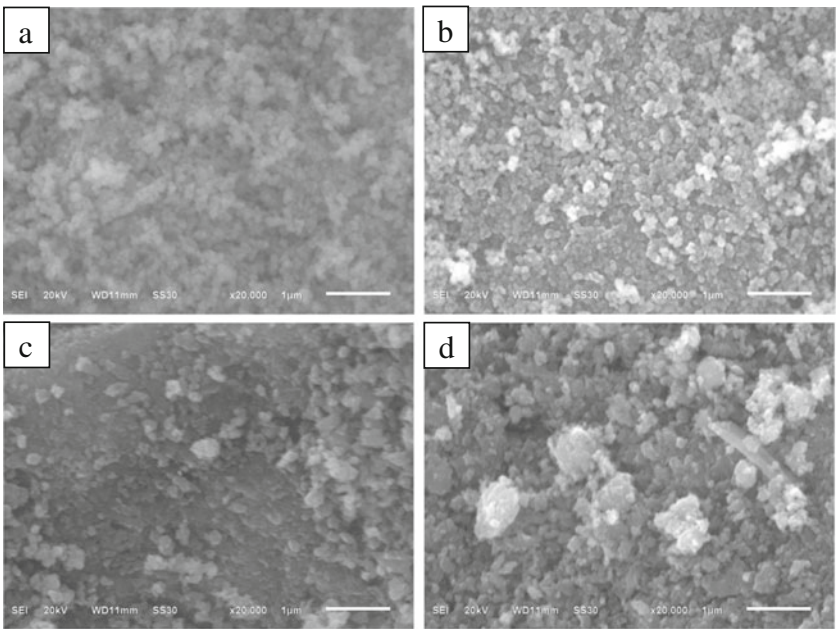

Fig. 5 SEM micrographs of **a** δ-MnO_2, **b** α-MnO_2, **c** γ-MnO_2, and **d** β-MnO_2

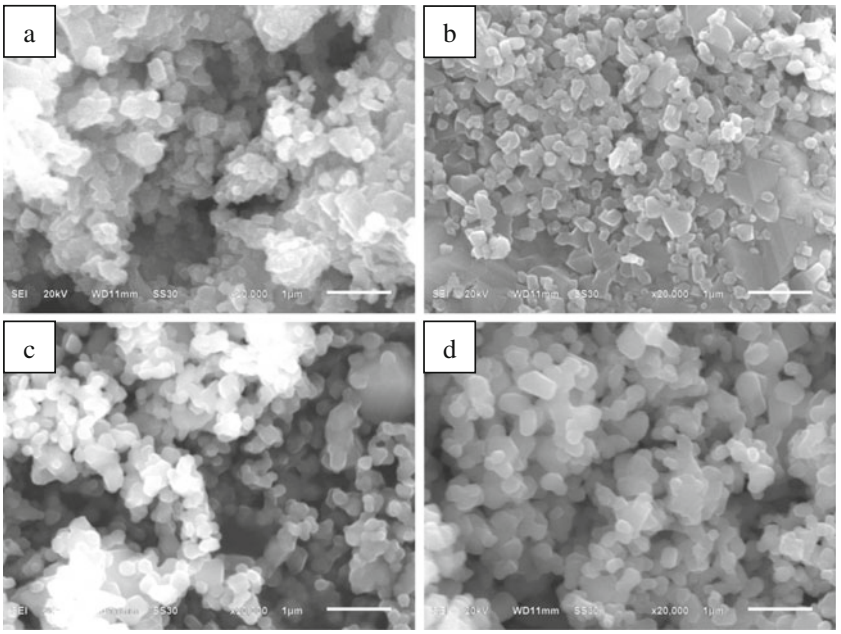

Fig. 6 SEM micrographs of $LiMn_2O_4$ prepared from (**a**) δ-MnO_2, (**b**) α-MnO_2, (**c**) γ-MnO_2, and (**d**) β-MnO_2

efficiencies can also be calculated as 95, 94, 92, and 97 % at the first cycle, respectively. The results indicate that the initial capacity and the coulombic efficiency of $LiMn_2O_4$ prepared by using β-MnO_2 as the manganese source are improved obviously.

In order to study the influence of different polymorphs of MnO_2 on the cycle performance of $LiMn_2O_4$, the batteries were tested at 0.5 C between 3.0 and 4.4 V at room temperature. The variation of the discharge capacity with the cycle number for $LiMn_2O_4$ powder prepared by using different manganese sources is shown in Fig. 8. It can be observed from Fig. 8 that the capacity retentions of different samples after 100 cycles are 40.8, 68.3, 77.8, and 83.3 %, respectively. Apparently, the $LiMn_2O_4$ obtained from β-MnO_2 represents a larger initial capacity and retains a higher capacity compared with the other three samples, while the $LiMn_2O_4$ obtained from δ-MnO_2 shows the poorest capacity retention.

To further study the evolution during the cycling tests, the charge/discharge curves of the first, 30th and 60th cycles of the samples are shown in Fig. 9. It is obvious that the sample prepared from β-MnO_2 (Fig. 9d) presents the highest stability during the cycling process, but for the other three samples, the capacity decreases rapidly and the polarization aggravates with the increase of cycle number, especially the sample prepared from δ-MnO_2 (Fig. 9a). In addition, the resulting operation voltage also decayed with cycling for the sample prepared from δ-MnO_2. It is considered that the variation is caused by the difference of the starting materials

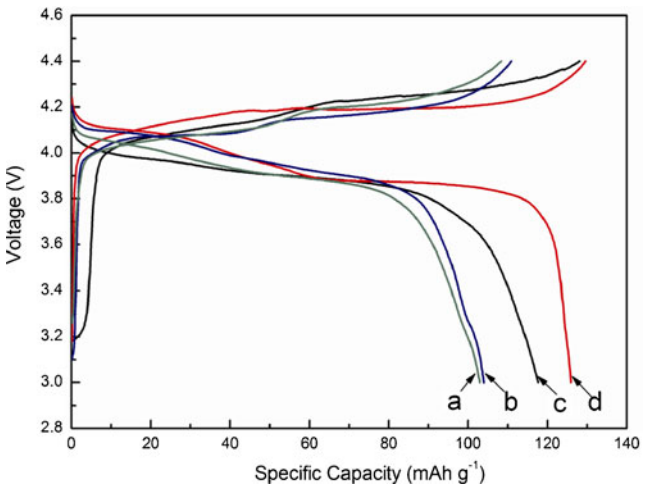

Fig. 7 Charge and discharge curves of $LiMn_2O_4$ prepared from (*a*) δ-MnO_2, (*b*) α-MnO_2, (*c*) γ-MnO_2, and (*d*) β-MnO_2 at rate of 0.5 C between 3.0 and 4.4 V

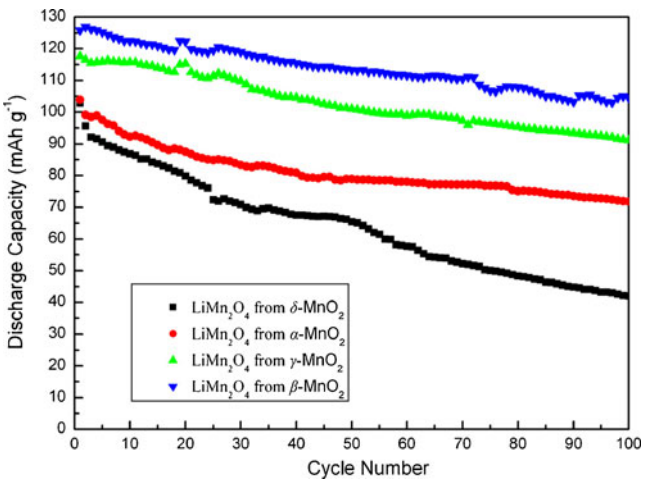

Fig. 8 Cycle performance of $LiMn_2O_4$ prepared from different polymorphs of MnO_2

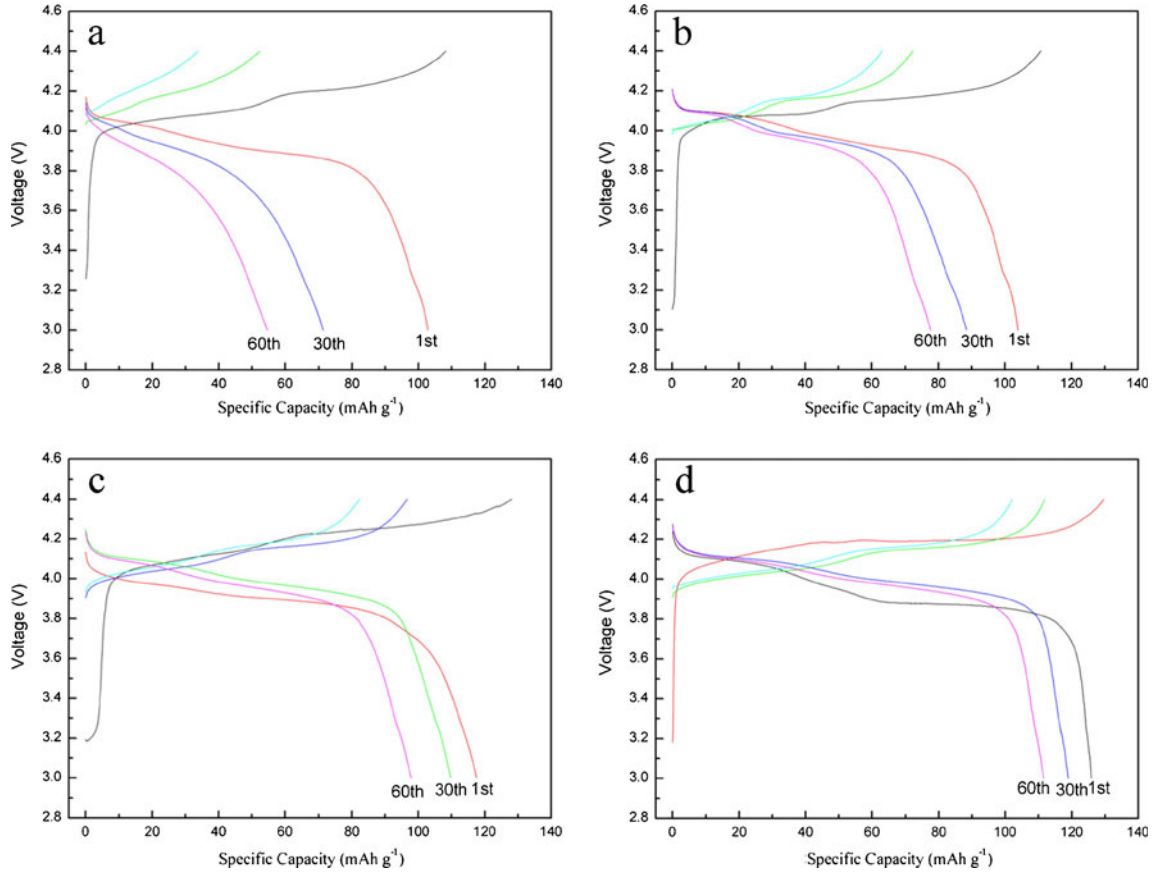

Fig. 9 The first, 30th and 60th charge–discharge curves of $LiMn_2O_4$ from **a** δ-MnO_2, **b** α-MnO_2, **c** γ-MnO_2, **d** β-MnO_2

under the same reacting conditions. Hence, β-MnO_2 may be a better alternative as the manganese source for the preparation of spinel $LiMn_2O_4$ as a cathode material for lithium-ion batteries.

The CVs for $LiMn_2O_4$ prepared from four different polymorphs of MnO_2 are displayed in Fig. 10. As exhibited, the curves of all samples have two pairs of symmetrical redox peaks, corresponding to the two pairs of charge and discharge plateaus shown in Fig. 7; the two pairs of redox peaks correspond to a two-step reversible intercalation reaction, in which Li^+ comes from two different tetragonal 8*a* sites of the spinel $Li_xMn_2O_4$ ($x<1$) at each step. The first oxidation peak is attributed to Li^+ removal from one-half of the tetrahedral sites; the second oxidation, the removal of Li^+ from the remaining tetrahedral sites, can be described as follows [40]:

$$\frac{1}{2}Li^+ + \frac{1}{2}e^- + 2MnO_2 \rightleftarrows Li_{0.5}Mn_2O_4 \quad (1)$$

$$\frac{1}{2}Li^+ + \frac{1}{2}e^- + Li_{0.5}Mn_2O_4 \rightleftarrows LiMn_2O_4 \quad (2)$$

The two redox peaks of the $LiMn_2O_4$ prepared from β-MnO_2 are narrow and well separated, and the narrow peak in the CV curve implies that a specific electrochemical reaction completes at a shorter period of time. But in other three samples, both the anodic and cathodic peaks become

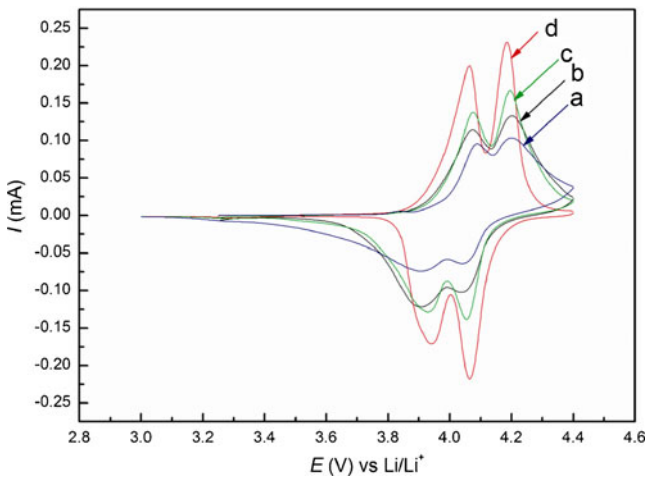

Fig. 10 Cyclic voltammograms of $LiMn_2O_4$ synthesized from (*a*) δ-MnO_2, (*b*) α-MnO_2, (*c*) γ-MnO_2, and (*d*) β-MnO_2 between 3.0 and 4.4 V. Scan rate=0.1 mV/s

Table 1 Electrochemical parameters from CV of different $LiMn_2O_4$ samples prepared from different polymorphs of MnO_2

Parameter	E_{a1}(V)	E_{a2}(V)	E_{r1}(V)	E_{r2}(V)	ΔE_{p1}(mV)	ΔE_{p2}(mV)
(a) δ-MnO_2	4.090	4.199	3.907	4.039	160	183
(b) α-MnO_2	4.074	4.201	3.909	4.038	163	165
(c) γ-MnO_2	4.075	4.196	3.927	4.055	141	148
(d) β-MnO_2	4.064	4.185	3.939	4.064	121	125

broad and low, the anodic peaks shift toward high potential and the cathodic ones shift toward low potential, suggesting the reversibility of the spinels decrease. The parameters obtained from Fig. 10 for the different samples are listed in Table 1. In comparison with the current peaks of the four samples, $LiMn_2O_4$ obtained from β-MnO_2 has less peak separations (ΔE_p), sharper and higher redox peaks, and shows well-defined splitting than the other three samples, which indicate that they have better cycle stability and lower overpotential. This result is in accordance with the charge/discharge curves (Fig. 9), and it also explains why the sample prepared from β-MnO_2 has the best electrochemical properties.

AC impedance spectroscopy is a powerful technique for determining kinetic parameters of the electrode process. It was carried out with three electrode cells after the cells had been charged and discharged at a 0.5 C current rate for a cycle, and the impedance plots have been fitted using the equivalent circuit model (Figs. 11 and 12). In general, The AC impedance pattern is composed of two partially overlapped semicircles in the high frequency region and sloping line in the low-frequency region. The intercept at the Z' axis in high frequency corresponds to the ohmic resistance (R_e), which represents the resistance of the electrolyte. The semicircle at middle frequency is correlated with the Li^+ charge transfer resistance at the interface [41], while the linear portion is designated to Warburg impedance (W), which is attributed to the diffusion of Li^+ into the bulk of the electrode materials. In this work, the R_e values are almost the same throughout the experiments due to the same electrolyte and fabrication parameters; they are much smaller than R_{ct}. The calculated parameters of R_{ct} values for the four kinds of $LiMn_2O_4$ are 83.01, 81.16, 80.19, and 61.38 Ω, respectively, indicating that the charge transfer resistance (R_{ct}) of $LiMn_2O_4$ from β-MnO_2 is less than those of other three products. Therefore, it suggests that the transfer rate of Li^+

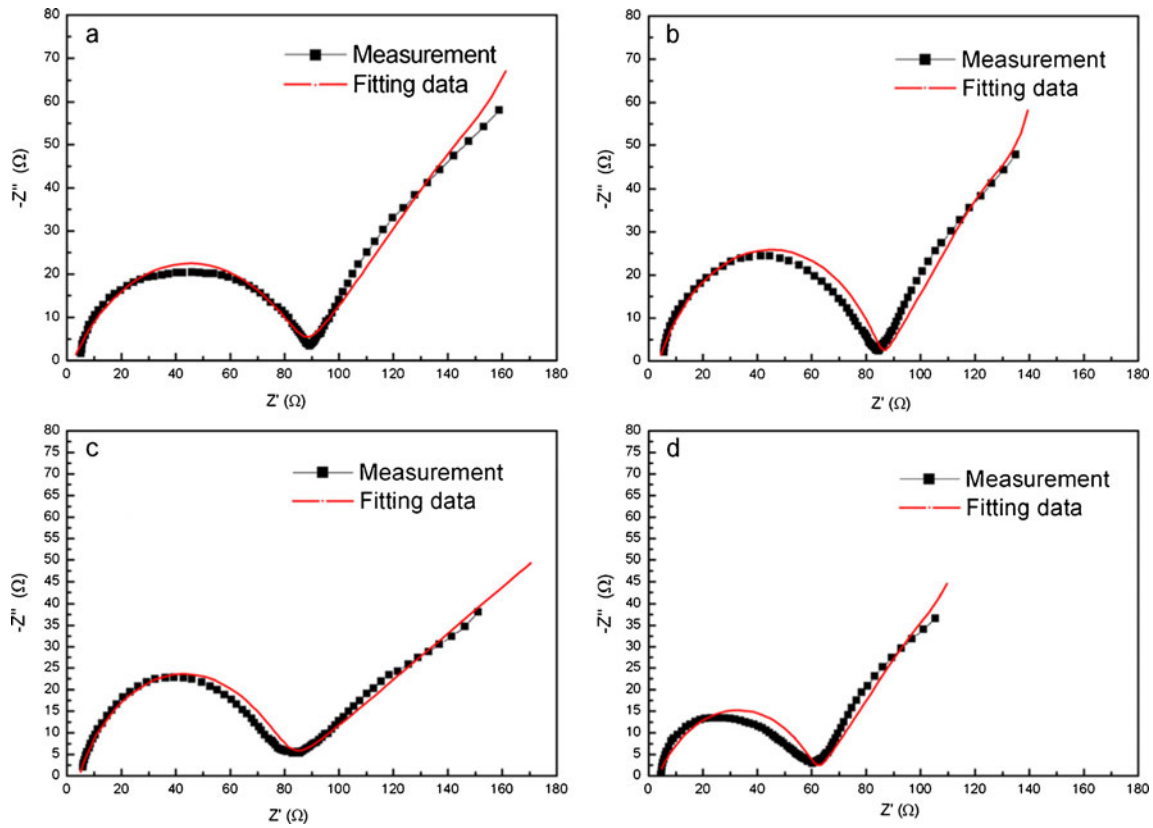

Fig. 11 Nyquist impedance spectra of $LiMn_2O_4$ synthesized from **a** δ-MnO_2, **b** α-MnO_2, **c** γ-MnO_2, and **d** β-MnO_2 from 0.01 Hz to 100 kHz

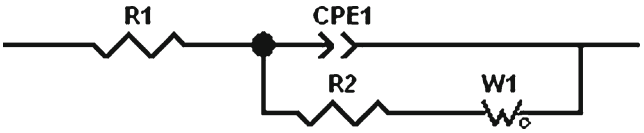

Fig. 12 Equivalent circuit for the impedance spectra

in the $LiMn_2O_4$ spinel structure is dramatically improved by using β-MnO_2 as the precursor.

As a consequence of the aforementioned comparison, an additional further testing was focused on battery characteristics of the $LiMn_2O_4$ prepared from β-MnO_2. Figure 13 displays the discharge capacity versus the cycle number for the $LiMn_2O_4$ sample prepared from β-MnO_2 at different current rates (0.5, 2, and 5 C). All three curves indicate good cycle ability and a high-rate capability. After 50 cycles, the 2 C discharge capacity could retain 91 % of the initial capacity. Besides, Shu et al. [17] reported that the discharge specific capacity of $LiMn_2O_4$ prepared from γ-MnOOH at 1 C rate was 110 mAh g^{-1}, and after 30 cycles, the discharge capacity maintained just 84.6 % of the initial capacity. Also, Kumar et al. [42] reported that the $LiMn_2O_4$ prepared from α-MnO_2 gave much higher capacities in lithium batteries than β-MnO_2, the reason can probably be ascribed to a poorer lithium uptake of β-MnO_2 phase during chemical lithiation. However, the $LiMn_2O_4$ prepared from β-MnO_2 in this work represents excellent electrochemical behaviors, because the $LiMn_2O_4$ samples were prepared by mixing different polymorphs of MnO_2 and Li_2CO_3 through one-step solid-state reaction, in which the Li content in $LiMn_2O_4$ are not affected by the lithium uptake of different polymorphs MnO_2.

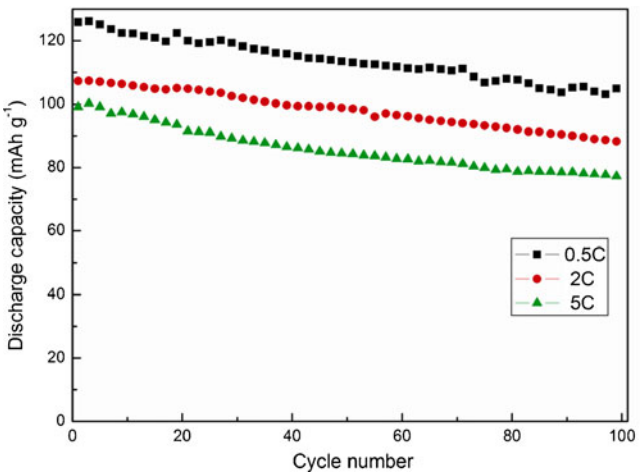

Fig. 13 Cycle performance of $LiMn_2O_4$ synthesized from β-MnO_2 at different charge–discharge rates

Conclusion

Spinel-phase cathode material $LiMn_2O_4$ samples for lithium-ion battery were synthesized by four different polymorphs of MnO_2 through one-step solid-state method. All the prepared $LiMn_2O_4$ have the same cubic spinel-phase structure without any impurities. Trace adsorbed oxygen was detected on the surface of the samples, the bond energy of Mn–O, and the average valence state of Mn is affected slightly by using different polymorphs of MnO_2 as the starting materials. The particle size and surface morphology of $LiMn_2O_4$ obtained from β-MnO_2 are well-distributed and more regular, and the sample prepared from β-MnO_2 exhibits the best electrochemical performance. These results, coupled with the low cost and environmentally benign nature of manganese, render β-MnO_2 as an attractive manganese source of $LiMn_2O_4$ with excellent electrochemical properties and battery characteristics.

Acknowledgments This work was financially supported by the National Natural Science Foundation of China under project No. 20871101, Joint Fund of Natural Science of Hunan Province and Xiangtan City under project No. 09BG005, and Project of Condition Research of Hunan Province under project No. 2010TC2004 Colleges.

References

1. Hosono E, Kudo T, Honma I, Matsuda H, Zhou HS (2009) Nano Lett 9:1045–1051
2. Jang DH, Shin YJ, Oh SM (1996) J Electrochem Soc 143:2204–2211
3. He XM, Li JJ, Cai Y, Wang YW, Ying JR, Jiang CY, Wan CR (2005) J Solid State Electrochem 9:438–444
4. Nakayama N, Nozawa T, Iriyama Y, Abe T, Ogumi Z, Kikuchi K (2007) J Power Sources 174:695–700
5. Li XF, Xu YL (2008) J Solid State Electrochem 12:851–855
6. Ouyang CY, Shi SQ, Lei MS (2009) J Alloys Compd 474:370–374
7. Lu W, Belharouak I, Park SH, Sun YK, Amine K (2007) Electrochim Acta 52:5837–5842
8. Komaba S, Oikawa K, Myung ST, Kumagai N, Kamiyama T (2002) Solid State Ionics 149:47–52
9. Xiao LF, Zhao YQ, Yanga YY, Cao YL, Ai XP, Yang HX (2008) Electrochim Acta 54:545–550
10. Hong YS, Han CH, Kim K, Kwon CW, Campet G, Choy JH (2001) Solid State Ionics 139:75–81
11. Ouyang CY, Zeng XM, Sljivancanin Z, Baldereschi A (2010) J Phys Chem C 114:4756–4759
12. Eftekhari A (2004) Solid State Ionics 167:237–242
13. Gnanaraj JS, Pol VG, Gedanken A, Aurbach D (2003) Electrochem Commun 5:940–945
14. Lee YS, Yoon CS, Sun YK, Yoshio M (2002) Electrochem Solid-State Lett 5:A1–A4
15. Zhang W, Liu Y, Yang Z, Tang S, Chen M (2004) Solid State Commun 131:441–445
16. Chabre Y, Pannetier J (1995) Prog Solid State Chem 23:1–130
17. Bao SJ, Li CM, Li HL, Luong JHT (2007) J Power Sources 164:885–889
18. Zhou WJ, Bao SJ, Liang YY, He BL, Li HL (2006) J Solid State Electrochem 10:277–282

19. Ha HW, Yun NJ, Kim K (2007) Electrochim Acta 52:3236–3241
20. Liang YY, Bao SJ, Li HL (2006) J Solid State Chem 179:2133–2140
21. Komaba S, Ogata A, Shimizu T, Ikemoto S (2008) Solid State Ionics 179:1783–1787
22. Guo H, Li X, Wang Z, Peng W, Cao X, Li H (2009) J Power Sources 189:95–100
23. Wan C, Nuli Y, Zhuang J, Jiang Z (2002) Mater Lett 56:357–363
24. Ferracin LC, Amaral FA, Bocchi N (2000) Solid State Ionics 130:215–220
25. Lee JW, Kim JI, Roh KC, Park SM, Kim K (2010) Solid State Sci 12:1687–1691
26. Cai J, Liu J, Suib SL (2002) Chem Mater 14:2071–2077
27. Komaba S, Sasaki T, Kumagai N (2005) Electrochim Acta 50:2297–2305
28. Patrice R, Dupont L, Aldon L, Jumas JC, Wang E, Tarascon JM (2004) Chem Mater 16:2772–2782
29. Thackeray MM, DeKock A, DePicciotto LA, Pistoia G (1989) J Power Sources 26:355–363
30. Momchilov A, Manev V, Nassalevska A (1993) J Power Sources 41:305–314
31. Thackeray MM (1997) Prog Solid State Chem 25:1–71
32. Yi TF, Hao CL, Yue CB, Zhu RS, Shu J (2009) Synthetic Met 159:1255–1260
33. Ragavendran K, Chou HL, Lu L, Lai MO, Hwang BJ, Ravi Kumar R, Gopukumar S, Emmanuel B, Vasudevan D, Sherwood D (2011) Mater Sci Eng B 176:1257–1263
34. Yu ZM, Zhao LC (2007) Trans. Nonferr Met Soc China 17:659–664
35. Li JG, Wang L, Zhang Q, He XM (2009) J Power Sources 189:28–33
36. Moses AW, Garcia Flores HG, Kim JG, Langell MA (2007) Appl Surf Sci 253:4782–4791
37. Shaju KM, Subba Rao GV, Chowdari BVR (2002) Solid State Ionics 152–153:69–81
38. Wei YJ, Yan LY, Wang CZ, Xu XG, Wu F, Chen G (2004) J Phys Chem B 108:18547–18551
39. Iwata E, Takahashi K, Maeda T, Mouri T (1999) J Power Sources 430:81–82
40. Armand M, Dalard F, Reroo D, Mouliom C (1985) Solid State Ionics 15:205–210
41. Gao F, Tang Z (2008) Electrochim Acta 53:5071–5075
42. Kumar VG, Gnanaraj JS, Salitra G, Abramov A, Gedanken A, Aurbach D, Soupart JB, Rousche JC (2004) J Solid State Electrochem 8:957–967